ORIGINAL RESEARCH ARTICLE

Structural, Electrical and Magnetic Properties of Copper-Substituted Co$_{0.8-X}$Ni$_{0.2}$ Ferrites Synthesized by Sol–Gel Autocombustion Process

Nabil Hamdi[1] · Wahid Belam[1]

Abstract

In this study, five Cu-Ni substituted cobalt ferrite nanoparticles, i.e., $Co_{0.8}Ni_{0.2}Fe_2O_4$; $Cu_{0.2}Co_{0.6}Ni_{0.2}Fe_2O_4$; $Cu_{0.4}Co_{0.4}Ni_{0.2}Fe_2O_4$; $Cu_{0.6}Co_{0.2}Ni_{0.2}Fe_2O_4$ and $Cu_{0.8}Ni_{0.2}Fe_2O_4$, have been prepared using an eco-friendly sol–gel auto-combustion process. The physicochemical characterization results derived from Fourier transform infrared (FTIR) spectroscopy, x-ray powder diffraction (XRPD), field emission scanning electron microscopy (FESEM), differential thermal analysis (DTA) and thermogravimetric analysis (TGA) have confirmed that the ferrite synthesized powders are pure and are formed by homogeneous crystallites varying in size from 19.96 nm to 24.94 nm. In addition, the nanosized ferrite cubic spinel basic framework has excellent stability versus copper substitution and thermal treatment beyond the combustion temperature and with no detection of tetragonal-cubic phase transition. Furthermore, the zero-field-cooled (ZFC)–field-cooled (FC) and magnetization versus magnetic field strength measurements using magnetization-hysteresis superconducting quantum interface device (M-H SQUID) magnetometry have proved the presence of superparamagnetic behavior at room temperature. Also, theoretical calculations of the superparamagnetic parameter have been performed by fitting the Langevin function to the M-H (300 K) data. The results indicate their significant dependence on both crystallite size and impact of copper composition. Indeed, during the substitution process, a decrease has been observed in remanence, saturation magnetization, coercivity, blocking temperature and magnetocrystalline values. The complex impedance spectroscopy (CIS) study has highlighted the best electrical conductivity value 18.07×10^{-3} S cm^{-1} associated with the lowest $E_a = 0.360$ eV of $Cu_{0.8}Ni_{0.2}Fe_2O_4$ at 373 K. The excellent magnetic and electrical features of the synthesized nanosized Cu-Ni substituted cobalt ferrites enable them to be applied in various nanotechnological fields of modern life.

Graphical Abstract
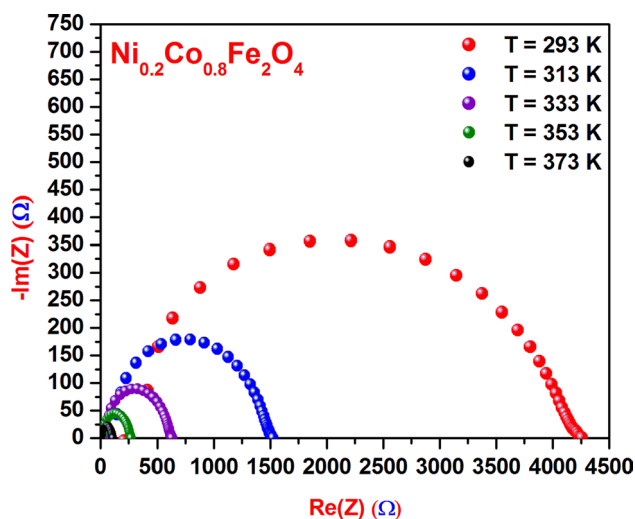
Extended author information available on the last page of the article

Introduction

Nowadays, the progress in research on magnetic, electric, and optical properties of ferrite nanoparticles is exponentially increasing, which is mainly due to their potential as candidates for application in various fields.[1,2]

In particular, the magnetic spinel nanoferrite system MFe_2O_4(M = Mn, Co, Ni, Cu, Zn) has attracted considerable attention of researchers in the last decade due to its distinctive physicochemical properties, including magnetic, optical, electrical and dielectric characteristics. Additionally, these nanoferrites exhibit excellent thermal and chemical stability, as well as good catalytic and photocatalytic properties with a moderate band gap value. The wide range of technological and biotechnological applications include magnetic drug delivery agents, detoxification, specific cell labeling, sonoimaging and MRI. These nanoferrites may also have application in photocatalysis, photoluminescence, biosensors, electrochemical gas sensors, humidity sensors, corrosion protection, water decontamination, magnetic liquids, permanent magnets, magnetic refrigeration, microwave technology, ceramic pigments, antimicrobial agents and hyperthermia in biomedicine.[3–7]

Indeed, the exceptional physicochemical properties of these nanoferrites are mainly due to the unique properties of the cubic spinel basic framework, which consists of two different geometrical configurations, normal and inverse spinel, which are derived from two different cationic distribution methods within tetrahedral (A) and octahedral (B) sites.[2] The network cohesion is ensured by the crystal field stabilization energy of the transition metal cations within these two sites.

In addition, most recent research has reported that the synthesis method, particle size, thermal treatment, and nature of the transition metal dopants are mainly considered as prominent factors that strongly affect the cationic distribution between the two sublattices labeled A and B compared to the normal occupancy within the cubic spinel basic structure. This leads to a considerable change in physicochemical properties of the nanoferrites.

In particular, many recent investigations have been focused on the most well-known cubic inverse spinel cobalt ferrite nanoparticles doped by different transitions metal dopants and synthesized by different methods,[8,9] in order to better understand their excellent physicochemical properties and their applications in the modern technology field.[10–18]

Recently, our new previous study has been devoted to the exploration of $Cu_XCo_{1-X}Fe_2O_4$(X = 0, 0.25, 0.5, 0.75, 1) ferrite nanoparticles, which represent the first series 1 (Y = 0),[2] derived from the parent system $Cu_XNi_YCo_{1-X-Y}Fe_2O_4$ ($0 \leq X \leq 1 - Y$; $0 \leq Y \leq 0.8$). Thus, the excellent magnetic and electrical properties of the five Cu substituted cobalt ferrite nanoparticles deduced from this study are encouraging in order to further investigate on the parent system. For this reason, the present work has been devoted to the second series 2 (Y = 0.2), which represents a continuation of the first series 1 (Y = 0).

The main purpose of this study is the synthesis of the five Cu-Ni substituted cobalt ferrite nanoparticles of series 2, $Cu_XCo_{0.8-X}Ni_{0.2}Fe_2O_4$ (X = 0, 0.2, 0.4, 0.6, 0.8), by the eco-friendly sol–gel autocombustion method and then highlight the influence of copper substitution at a fixed composition of Ni^{2+}(Y = 0.2) on the structural, electrical and magnetic properties by physicochemical characterization techniques including differential thermal analysis with thermogravimetric analysis (DTA-TGA), x-ray powder diffraction (XRPD), Fourier transform infrared (FTIR) spectroscopy, complex impedance spectroscopy (CIS), zero-field-cooled (ZFC)–field-cooled (FC) and magnetometry using a magnetization-hysteresis superconducting quantum interference device (M-H SQUID). We also aim to determine the superparamagnetic parameters by fitting Langevin function theoretical calculations using M-H (300 K) data.

Experimental Techniques

Chemical Synthesis Process

The sol–gel preparation of the five Cu-Ni substituted cobalt ferrites was performed using a mixture of basic reactants (Sigma Aldrich), including citric acid, cobalt(II) nitrate hexahydrate, nickel(II) nitrate hexahydrate, copper(II) nitrate trihydrate, and iron(III) nitrate nonahydrate, with purity values of 99.5%, 99%, 99%, 99%, 98%, respectively. The reactants were measured in the stoichiometric proportion of each corresponding composition with a suitable amount of distilled water under magnetic stirring. Citric acid was added to the last reaction mixture in a 1:1 molar ratio to the metal cations as an eco-friendly metal chelating agent and autocombustion fuel. Then, the resulting aqueous solutions of each studied composition X were heated at 353 K under stirring, followed by the adjustment of pH value to

7 using a suitable volume of concentrated ammonia solution. This caused the formation of viscous black gel, which transformed into fractal loose precursor powders after reaching the corresponding autocombustion temperatures below 523 K. Then, the precursor powders were ground slightly and then calcined at 550 K for 2 h leading to the synthesis of five nanosized Cu-Ni substituted cobalt ferrites, $Co_{0.8}Ni_{0.2}Fe_2O_4$, $Cu_{0.2}Co_{0.6}Ni_{0.2}Fe_2O_4$, $Cu_{0.4}Co_{0.4}Ni_{0.2}Fe_2O_4$; $Cu_{0.6}Co_{0.2}Ni_{0.2}Fe_2O_4$; $Cu_{0.8}Ni_{0.2}Fe_2O_4$, which correspond to the five X compositions 0; 0.2; 0.4; 0.6; 0.8, and were labeled S2M1–5.

Physicochemical Characterization Procedures

Thermograms using coupled differential thermal analysis (DTA) and thermogravimetric analysis (TGA) of the five dried gel precursors were recorded using a SETARAM TGA92 thermal analyzer in a temperature range from room temperature to 1173 K at a heating rate of 10 K min^{-1} under an argon atmosphere.

A Bruker D8 Advance diffractometer, using 1.54187 Å Cu-Kα radiation, was used to record the five 298 K diffractograms of the studied ferrites S2M1-5 in the 10–100° 2θ diffraction angle range with 0.02° scan step width and 16 s scanning time per step.

The Fourier transform infrared (FTIR) spectral data were recorded using a NICOLET IR 200 FTIR spectrometer in the sweeping range 400–4000 cm^{-1}. Complex impedance spectroscopy (CIS) was used to study the electrical conductivity properties. The experimental data acquisition was carried out using a Solartron SI 1260 analyzer in the frequency range between 10 Hz and 32 MHz, recording 10 measurements per decade per frequency interval, under 100 mV imposed voltage. The cylindrical

The zero-field-cooled (ZFC)–field-cooled (FC) and magnetization versus applied magnetic field (M-H) were measured using a Quantum Design MPMS superconducting quantum interface device (SQUID) magnetometer under 500 Oe imposed magnetic field and in the 10–300 K temperature range.

The surface morphology and elemental composition of the five explored nanoferrites were analyzed using a Carl-Zeiss MERLIN field emission scanning electron microscope (FESEM) coupled with energy dispersive x-ray (EDX) spectroscopy with a high resolution of 0.8 nm and 1.4 nm at 15 kV and 1 kV, respectively.
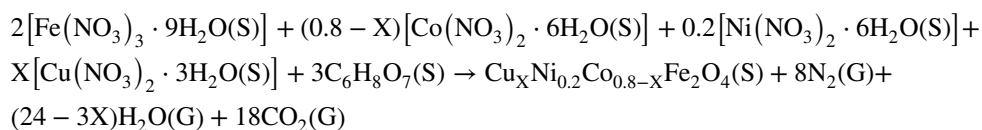
Results and Discussion

DTA-TGA

As shown in Fig. 1 and the upper right inset, the DTA-TGA thermograms of the five studied nanoferrites S2M1-5 have similar profiles and each one exhibits in the TGA curve only a single mass loss, around $\Delta m \approx -5\%$, which was confirmed in the corresponding DTA curve, by the presence of a narrow exothermic peak which is ascribed to the autocombustion phenomenon.

Indeed, the observed exothermic peak at the combustion temperature (T_C), is attributed to the autocombustion chemical reaction between iron, cobalt, nickel and copper nitrates, and citric acid as organic combustibles, and this leads to the synthesis of the corresponding highly crystalline single phase cubic spinel ferrite according to the following chemical equation:

where $X = 0, 0.2, 0.4, 0.6, 0.8$.

The chemical equation was written according to the propellant chemistry principle,[19] by considering that the

$$2\left[Fe(NO_3)_3 \cdot 9H_2O(S)\right] + (0.8 - X)\left[Co(NO_3)_2 \cdot 6H_2O(S)\right] + 0.2\left[Ni(NO_3)_2 \cdot 6H_2O(S)\right] +$$
$$X\left[Cu(NO_3)_2 \cdot 3H_2O(S)\right] + 3C_6H_8O_7(S) \rightarrow Cu_XNi_{0.2}Co_{0.8-X}Fe_2O_4(S) + 8N_2(G) +$$
$$(24 - 3X)H_2O(G) + 18CO_2(G)$$

pellet of each studied ferrite was compacted uniaxially under 120 MPa pressure and then sintered at 1173 K for 24 h. Gold deposition was performed by vacuum evaporation on both sides of each pellet with 13-mm diameter in order to ensure that the electrode had good ohmic contact. The recorded Nyquist diagram data was measured in the temperature range from 293 to 373 K with increments of 20 K.

combustion reaction products are primarily constituted by CO_2, N_2 and H_2O.

Moreover, beyond the combustion temperature and until 1173 K, no thermal phenomenon was detected in the five thermograms. Indeed, the thermal behavior of the five Cu-Ni substituted cobalt ferrite single phases shows an excellent stability without any phase transition below 1173 K, which leads to the estimation of the appropriate calcination temperature range of 550–1173 K.

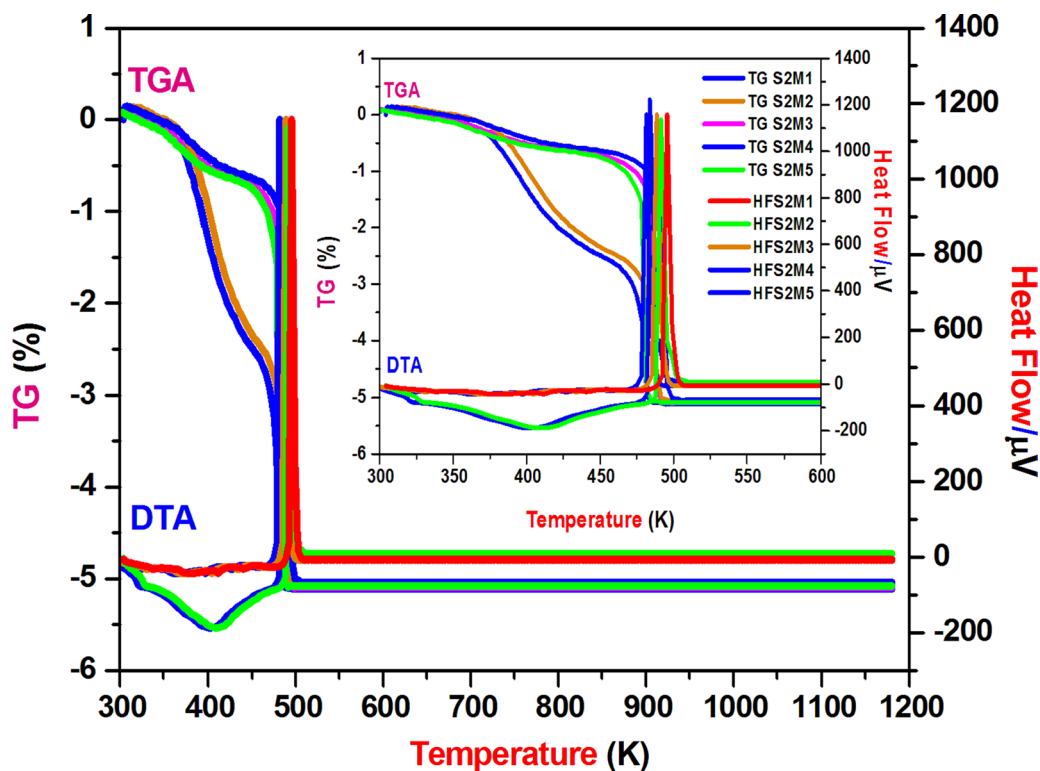**Fig. 1** DTA-TGA thermograms of nanosized ferrites S2M1-5.

In addition, at constant value of molar number for both nickel n(Ni) = 0.2 and citric acid n(C$_6$H$_8$O$_7$) = 3, from 494.96 K to 502.75 K, the observed increase in the value of T_C, of the five Cu-Ni substituted cobalt ferrites, S2M1 (T_C = 494.96 K), S2M2 (T_C = 496.90 K), S2M3 (T_C = 498.85 K), S2M4 (T_C = 500.81 K), S2M5 (T_C = 502.75 K), increase with copper content, which has a higher atomic mass than cobalt, and may be assigned to the molecular mass increase from M(S2M1) = 234.57 g mol^{-1} to M(S2M5) = 238.26 g mol^{-1}.

Furthermore, the thermogram profiles of the five synthesized nanoferrites are similar to those reported in similar work devoted to M$_{0.5}$Co$_{0.5}$Fe$_2$O$_4$ (M = Ni, Cu, Zn), elaborated by the same synthesis process used herein, and their combustion temperatures have been observed around 473 K.[20]

X-ray Powder Diffraction Analysis

In order to avoid the formation of grain growth and agglomeration, the five samples were calcined at 550 K for 2 h.

The five profiles of the recorded x-ray powder diffractograms of the studied ferrites shown in Fig. 2 are similar and show clearly the presence of only sharp peaks of single-phase crystalline nature confirming the spinel basic structure of the corresponding five Cu-Ni substituted nanosized cobalt
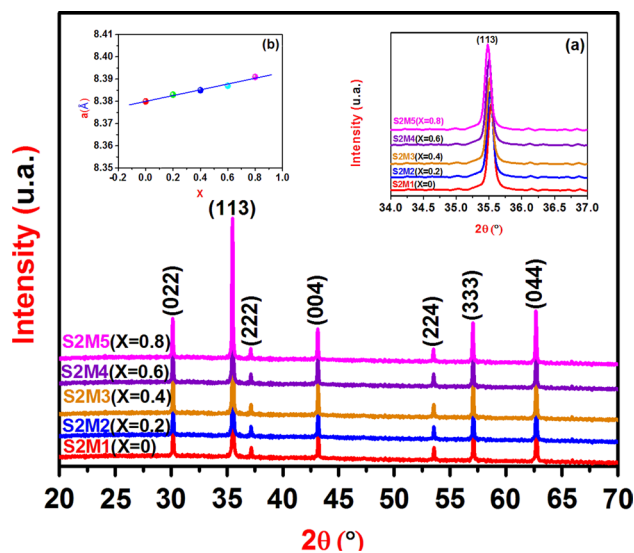

Fig. 2 XRP diffractograms of nanosized ferrites S2M1-5, (a) Zoomed-in Bragg reflection (1 1 3) of the nanosized ferrites S2M1-5 and (b) Graphic representation of the a lattice parameter versus the Cu content of nanosized ferrites S2M1-5.

ferrites S2M1-5. Moreover, the measured diffraction peaks of the as-synthesized ferrites have been perfectly indexed in the cubic system with Fd$\overline{3}$m space group in accordance with

Table I Refined lattice parameters and crystallite size calculations of the nanosized ferrites S2M1-5

| Nanoferrite	a (Å)	Space group	D_{XRPD} (nm)
S2M1 ($X = 0$)	8.380(1)	$Fd\bar{3}m$	18.77
S2M2 ($X = 0.2$)	8.383(4)	$Fd\bar{3}m$	19.97
S2M3 ($X = 0.4$)	8.385(2)	$Fd\bar{3}m$	20.51
S2M4 ($X = 0.6$)	8.387(5)	$Fd\bar{3}m$	21.60
S2M5 ($X = 0.8$)	8.391(3)	$Fd\bar{3}m$	23.39

data derived from JCPDS card file no. 79-1744 of spinel $CoFe_2O_4$.

As a result, the collected data results derived from the x-ray diffraction analysis indicate the high purity of the five studied powder compositions and perfectly proved the remarkable stability of the cubic spinel crystalline structure during the replacement of Co by Cu cations within the parent $CoFe_2O_4$ basic framework, meanwhile, copper content X increases from 0 to 0.5 and Ni composition Y remains constant equal to 0.2.

Furthermore, the lattice parameter values have been refined by linear regression using the least square fit method performed by CELREFF software,[21] which uses hkl with their corresponding $2\theta(°)$ values by importing the raw format acquisition data. The five refined lattice parameters are depicted in Table I. In addition, the five diffractograms of various compositions show that the XRPD peaks seem to be slightly displaced toward lower values of 2θ diffraction angles in comparison with those of cobalt ferrite diffractogram when copper composition X increases from 0 to 0.8 at constant nickel content $Y = 0.2$. Indeed, in the case of Bragg reflection (1 1 3), Fig. 2a shows a slight shift of 2θ value from 35.52° [$X = 0$] to 35.47° [$X = 0.8$], which is due to the low growth in the lattice constant from a[$X = 0$] = 8.380(1) Å to a[$X = 0.8$] = 8.391(3) Å, Table I. This result can be explained on the basis of the small difference between cationic radius values of Cu^{2+} and Co^{2+}: r(Cu^{2+}) = 0.73 Å and r(Co^{2+}) = 0.72 Å, respectively.

The lattice parameter variation with copper content X is shown in Fig. 2b. In fact, the lattice parameter value varies linearly with Cu composition increase and thus indicates that the Cu-Ni substituted cobalt ferrite system obeys Vegard's law,[22] by the following fitted equation: a(X) = 8.380 + 13.10^{-3}X, which is obtained from the linear fit of the graphical representation of the a lattice parameter as function of Cu content X. In addition, a similar behavior of lattice parameter increase with dopant content has been reported by many investigators in various studies devoted to several metallic cation substituted cobalt ferrite.[23]

Additionally, even though the copper composition is equal to 0.8, the room temperature diffractogram of $Cu_{0.8}Ni_{0.2}Fe_2O_4 (X = 0.8)$ indicates that the nanoferrite
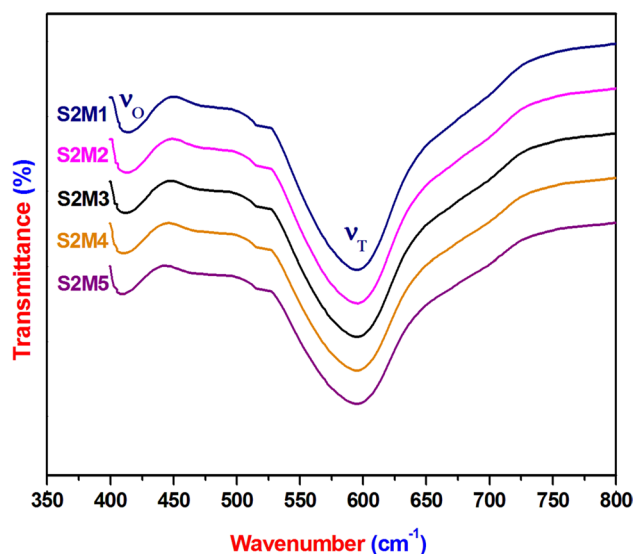
Fig. 3 FTIR Zoomed spectra of nanosized ferrites S2M1-5.

crystallizes in the cubic spinel system with the space group $Fd\bar{3}m$ and with no detection of tetragonal phase transition with the space group $I4_1/amd$, which is cited in the case of $CuFe_2O_4$.[24] Indeed, this result confirms that copper cations preferentially occupy the octahedral sites, within the classic spinel lattice, instead of the tetrahedral sites during the substitution process.

Moreover, the calculation of crystallite grain size D has been performed using Scherrer's relation[25] whose different variables and constants have been detailed in our recent research paper.[2]

$$D = \frac{0.9\lambda}{\Delta(2\theta)\cos\theta}$$

The data listed in Table I show that the nanocrystallinity of the five studied ferrites has been highlighted by the crystallite grain size calculation values which are less than 100 nm and whose values seem to increase with Cu content X from $D_{XRPD}[Co_{0.8}Ni_{2.0}Fe_2O_4]$ = 18.77 nm to $D_{XRPD}[Cu_{0.8}Ni_{0.2}Fe_2O_4]$ = 23.39 nm. The structural properties deduced from the XRPD study is in coherence with those reported in similar investigations.[2,21,22]

FTIR Vibrational Characterization

Fourier transform infrared spectroscopy study has been performed for further additional information concerning the crystalline framework. As shown in Fig. 3, the five vibrational spectra of the explored nanosized ferrites reveal the presence of two principal absorption peaks situated at the wavenumber values 595 cm^{-1} and 412 cm^{-1}, which are assigned to the tetrahedral and octahedral vibration modes
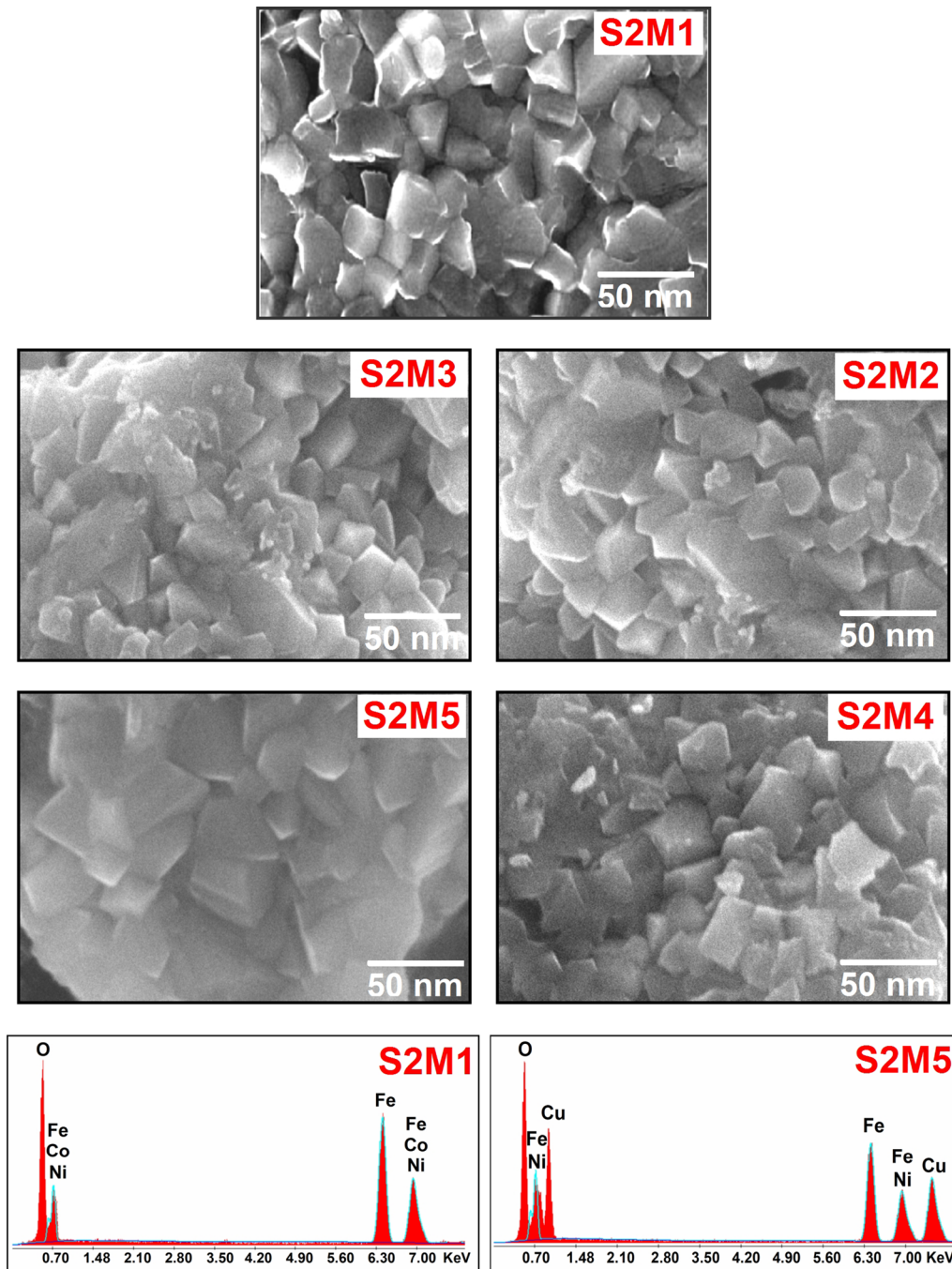
Fig. 4 FESEM micrographs of nanosized ferrites S2M1-5.

corresponding to the single phase cubic inverse lattice.[25,26] The obtained values from the experimental spectra of tetrahedral and octahedral absorption bands are in good agreement with those reported in similar works.[26,27]

In addition, on the same point view, it can be concluded that the results derived from the thermogravimetric, FTIR and XRPD studies are in good accordance that the five

Cu-Ni-Co nanosized ferrites are pure and their lattice parameters correspond to the cubic spinel crystal structure.

FESEM Analysis

The observed morphologies of the five studied nanoferrites derived from the FESEM micrographs depicted in Fig. 4 show a uniform grain size distribution with angular

Table II EDX elemental analyses of the nanoferrites S2M1-5

Nanoferrite	Atomic percentage (%)				
	Co	Cu	Ni	Fe	O
S2M1 $Co_{0.8}Ni_{0.2}Fe_2O_4$	11.57	–	2.79	28.54	56.87
S2M2 $Co_{0.6}Cu_{0.2}Ni_{0.2}Fe_2O_4$	8.65	2.93	2.92	28.47	56.93
S2M3 $Co_{0.4}Cu_{0.4}Ni_{0.2}Fe_2O_4$	5.78	5.82	2.74	28.39	56.78
S2M4 $Co_{0.2}Cu_{0.6}Ni_{0.2}Fe_2O_4$	2.86	8.64	2.81	28.43	56.84
S2M5 $Cu_{0.8}Ni_{0.2}Fe_2O_4$	–	11.51	2.75	28.61	56.71
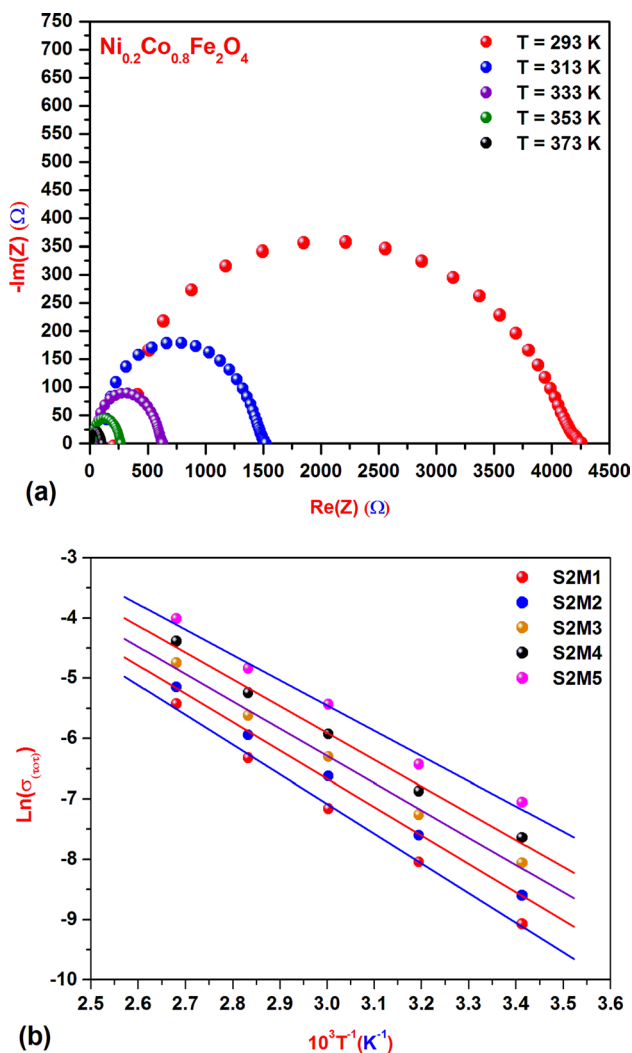
Fig. 5 (a) Impedance diagram of the nanosized ferrite S2M1 in the temperature range 293–373 K and (b) Arrhenius plot of nanosized ferrites S2M1-5.

shapes, whose grain sizes vary from $D_{FESEM} = 20.86$ nm to $D_{FESEM} = 25.62$ nm. As a consequence, these values seem to be slightly higher than those determined by Langevin function fitting D_{LFF} and Scherrer's equation D_{XRPD}. Thus, the observed grain size difference between D_{FESEM} and D_{LFF} can

be attributed to the presence of dead magnetic layers inside the structure of the five nanoferrites.[28] The EDX analysis results of elemental composition of the five as-synthesized ferrite nanoparticles listed in Table II closely match the corresponding stoichiometric ratios used for the synthesis.

Electrical Characterization by CIS

The impedance diagrams of the five nanosized ferrites recorded at 293 K, 313 K, 333 K, 353 K and 373 K have similar profiles. As shown in Fig. 5a, the Nyquist diagram of S2M1 [$X = 0$] exhibits only one semicircular arc which confirms that the electrical conduction behavior within the studied ferrite framework is principally due to the bulk resistance with a total absence of grain boundary effect.[29] The calculation of direct current conductivity value has been carried out by the following relation: $\sigma_{DC} = E/R_{DC}S$, wherein E is the thickness of pellet and S its corresponding surface. At fixed temperature, the values of bulk resistance may be determined by intersection of the corresponding semicircle with the real axis in the Nyquist diagram.

Figure 5b represents the Arrhenius plots of $\ln(\sigma_{DC})$ as a function of $10^3/T$ of the five Cu-Ni-Co nanosized ferrites, which exhibit a perfect linear fit trend of Arrhenius equation $\sigma_{Tot} = \sigma_0 \exp(-E_a/K_B T)$, wherein T, K_B, E_a and σ_0 are the absolute temperature, the Boltzmann constant, the electrical conduction activation energy and the pre-exponential factor, respectively.
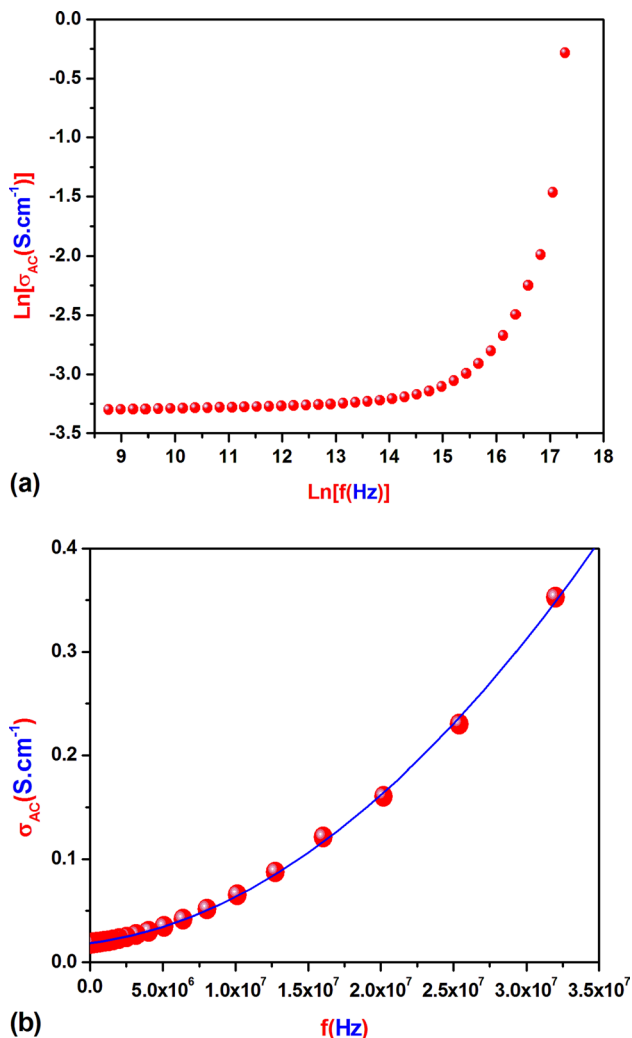
The observed increase in electrical conductivity versus temperature is a clear indication that the electrical conduction behavior is a thermally activated process leading to the calculation of E_a for each nanosized ferrite from its plot slope determined from the electrical data linear fit. The illustrated electrical properties in Table III are in good coherence with those cited in similar study data;[30–34] however, at constant copper content X, the DC electric conductivity value of each studied nanosized ferrite increases as temperature increases from 293 K to 373 K.

Moreover, the DC conductivity value of $Co_{0.8}Ni_{0.2}Fe_2O_4$ [$X = 0$] and $Cu_{0.8}Ni_{0.2}Fe_2O_4$ [$X = 0.8$] increases by 38 and 21 orders of magnitude, respectively. The S2M5 nanosized ferrite exhibits the highest DC electrical conductivity value $\sigma_{DC}(373\ K) = 1.807 \times 10^{-3}$ S cm^{-1} with lower associated activation energy of 0.360 eV, and this observation can be explained by the increase of electrical charge carrier drift mobility, which clearly indicates the presence of semiconductor-like behavior.

In addition, at 293 K and 373 K fixed temperature, the DC electrical conductivity value increases more than seven and four orders of magnitude, respectively, as copper composition increases. In fact, the observed electrical conductivity growth with the increase of Cu content X from 0 to 0.8, at fixed Ni composition $Y = 0.2$, is mainly due to the

Table III Electric properties of the nanosized ferrites S2M1-5

Nanoferrite	$\sigma_{DC(293\ K)}$ (S cm^{-1})	$\sigma_{DC(313\ K)}$ (S cm^{-1})	$\sigma_{DC(333\ K)}$ (S cm^{-1})	$\sigma_{DC(353\ K)}$ (S cm^{-1})	$\sigma_{DC(373\ K)}$ (S cm^{-1})	E_a (eV)
S2M1	1.151×10^{-4}	3.214×10^{-4}	7.762×10^{-4}	0.00179	0.0044	0.423
S2M2	1.847×10^{-4}	5.006×10^{-4}	0.00133	0.00263	0.00582	0.403
S2M3	3.158×10^{-4}	7.013×10^{-4}	0.00184	0.00363	0.00867	0.388
S2M4	4.812×10^{-4}	0.00103	0.00267	0.00529	0.01247	0.382
S2M5	8.632×10^{-4}	0.00162	0.00436	0.00794	0.01807	0.360

Fig. 6 (a) Graphic representation of $Ln(\sigma_{AC})$ versus $Ln(f)$ of nanosized ferrite S2M5 and (b) Second-order polynomial fitted curve of $\sigma_{AC}(373\ K)$ versus frequency of nanosized ferrite S2M5.

Furthermore, the study of AC conductivity σ_{AC} evolution in the frequency domain from 10 Hz to 32 MHz, has been performed for further investigation on electrical properties and then leading to the conduction mechanism identification. Indeed, the study has been focused on $Cu_{0.8}Ni_{0.2}Fe_2O_4$ which has the highest DC electric conductivity value at 373 K. As shown in Fig. 6a, which represents the $ln(\sigma_{AC})$ curve versus $ln(f)$, the presence of a linear zone in the low frequency domain immediately accompanied by an exponential growth of plot with a frequency in the higher frequency range is an indication that the mechanism of AC electrical conduction within the ferrite framework depends on both temperature and frequency, and consequently obeys Jonsher's universal power law equation, $\sigma_{AC} = \sigma_{DC} + P\omega^n$, where n is the angular frequency exponent, ω is the angular frequency and P is a temperature-dependent constant.[35]

In addition, the second-order polynomial fitted curve of $\sigma_{AC}(373\ K)$ as a function of frequency of the $Cu_{0.8}Ni_{0.2}Fe_2O_4$ nanoferrite, shown in Fig. 6b, has been used to calculate the fitted values of $\sigma_{DC}(373\ K) = 0.0182(3)$ S cm^{-1}, $P(373\ K) = 4.275\times10^{-18}$ S cm^{-1} rad^{-1} and $n = 2$, with an R-squared value equal to 0.9994, and it can be deduced that the fitted 300 K DC electrical conductivity value, 0.0182(3) S cm^{-1}, is almost equal to that determined from the 373 K recorded Nyquist diagram data of S2M5 nanoferrite, $\sigma_{DC}(373\ K) = 0.01807$ S cm^{-1}. As a result, inside the 3-D framework system of the explored Cu-Ni substituted cobalt ferrite nanoparticles, the charge carrier transport is occurred by the mutual electron hopping exchange between ferric Fe^{3+} and ferrous Fe^{2+} cations which are distributed in random equivalent sublattice sites in the imposed electrical field direction.[1,36,37]

Magnetic Characterization by SQUID Magnetometry

The ZFC–FC magnetization curves with similar profiles, shown in Fig. 7a, drawn from the recorded data in the temperature range from 10 K to 300 K and under an applied magnetic field of 500 Oe, have been used to interpret the magnetic behavior and to determine the blocking temperature of each magnetic ferrite, T_B, from the first particular point deduced from the beginning of the corresponding curve.

electrical property difference between copper and cobalt, which have elementary electrical conductivity values of 0.294 S cm^{-1}, 0.172 S cm^{-1}, respectively, leading to the conductivity enhancement by increasing the charge carrier concentration when Cu concentration increases from 0 to 0.8. Consequently, there is a decrease in the E_a value from 0.423 eV to 0.360 eV.
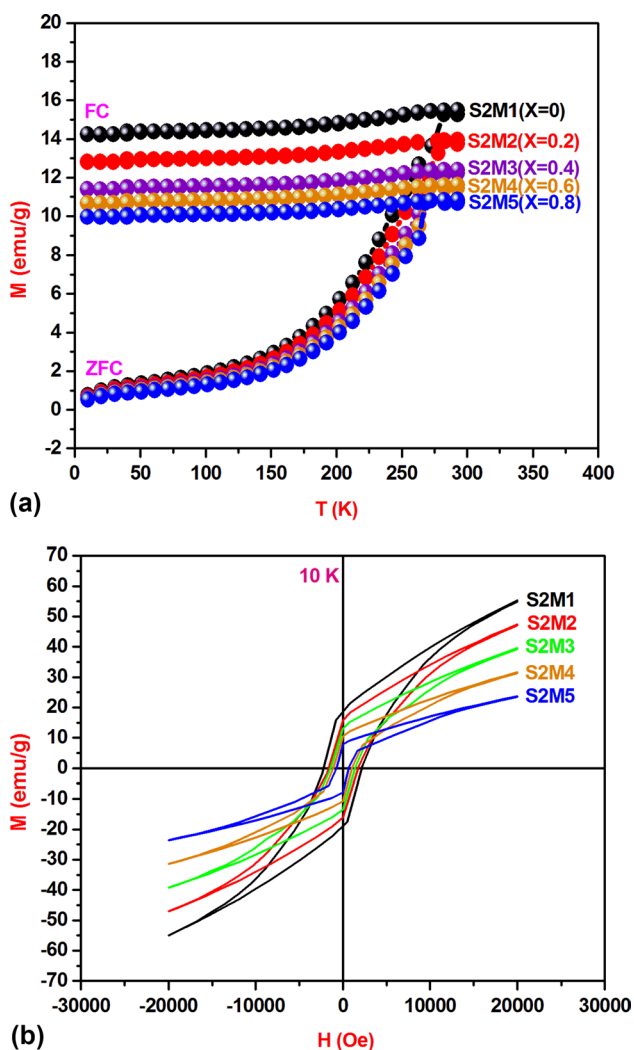
Fig. 7 (a) The ZFC–FC magnetization curves of the nanosized ferrites S2M1-5 recorded in the temperature range 10–300 K and under 500 Oe magnetic field and (b) the 10 K hysteresis loops of the nanosized ferrites S2M1-5.

The deduced blocking temperature T_B of the five nanosized ferrites, S2M1-5, are $T_B(X = 0) = 282.21$ K; $T_B(X = 0.2) = 277.97$ K; $T_B(X = 0.4) = 274.30$ K; $T_B(X = 0.6) = 270.92$ K and $T_B(X = 0.8) = 267.85$ K. However, at constant composition of nickel Y = 0.2, the observed decrease in the T_B value from 282.21 K to 267.85 K, with the increase of Cu content X from 0 to 0.8, can be explained by the fact that at $X = 0$, the starting nanosized ferrite, $Ni_{0.2}Co_{0.8}Fe_2O_4$, has a cubic inverse spinel basic structure within which the Fe^{3+} transition metal cations are ensnared in a weak ligand field which is due to the presence of high spin states generated by the $3d^5$ electronic configurations.

The magnitude contribution of magnetic anisotropy is mainly established from the strong L-S coupling of Co^{2+} transition metal cations due to their $3d^7$ electronic configurations. In fact, the presence of Co^{2+} cations in the octahedral sites create a high magnetocrystalline anisotropy and induce a large energy barrier value of magnetocrystalline anisotropy K. In addition, the observed decrease in the energy barrier value of magnetocrystalline anisotropy K from 4.87×10^5 erg cm^{-3} to 2.01×10^5 erg cm^{-3} with the decrease of Co composition from 0.8 to 0 is primarily due to the substitution within the octahedral sites of Co^{2+} cations which have higher L-S coupling contribution by Cu^{2+} cations with a lower one, leading to the observed decrease in the T_B value with Cu composition and particle size increase. In fact, these obtained results are in good agreement with the following relation: $T_B = \frac{KV}{25K_B}$, which shows clearly the relationship between T_B and K reported hereafter.

Furthermore, the existence of the intersection between ZFC–FC magnetization curves clearly confirms the room temperature transition of the five magnetic nanoferrites from the ferrimagnetic blocked regime to the superparamagnetic regime, which imposes a dominant magnetic single domain, in which the thermal energy value K_BT becomes larger than that of the magnetic anisotropy energy barrier thus causing the deblocking of the switchability of the magnetic moment towards the magnetic applied field inducing the superparamagnetic regime transition according to the Curie–Weiss law.[38,39]

Moreover, the five similar ZFC curves display a saturation trend confirmed by the presence of a linear zone extending from 10 K to 150 K, immediately followed by an exponential increase until reaching the blocking temperature. On the other hand, the tendency to saturation has also been observed in the ZF magnetization curve of the five magnetic ferrites, which indicates the presence of strong dominant dipolar interactions between the A and B metallic transition cations inserted in the tetrahedral and octahedral crystallographic sites, respectively.[40] As a result, this characteristic superparamagnetic behavior has been reported in similar recent studies devoted to ferrite nanoparticles.[41]

Figure 7b presents the magnetic hysteresis loops recorded at 10 K and clearly shows that the five ferrimagnetic nanosized ferrites are in the blocked magnetic state, and as a result, they obey Stoner-Wolhfarth's law,[42] while the recorded 300 K M-H curves, shown in Fig. 8a, indicate the presence of superparamagnetic behavior characterized by a dominant magnetic single domain, which is confirmed by the absence of a hysteresis loop in the 300 K M-H curves. Additionally, the observed reduction in saturation magnetization M_S values at 300 K in comparison with those at 10 K can be assigned to the magnetic moment distribution under the imposed field direction which is strongly related to the common concurrence between the thermal and magnetocrystalline anisotropy energies versus temperature.

In fact, beyond the blocking temperature T_B, the dominant magnetic moment becomes randomly oriented, and as a result, the magnetocrystalline anisotropy energy value becomes lower than that of thermal energy, thus inducing the transition to the superparamagnetic regime.
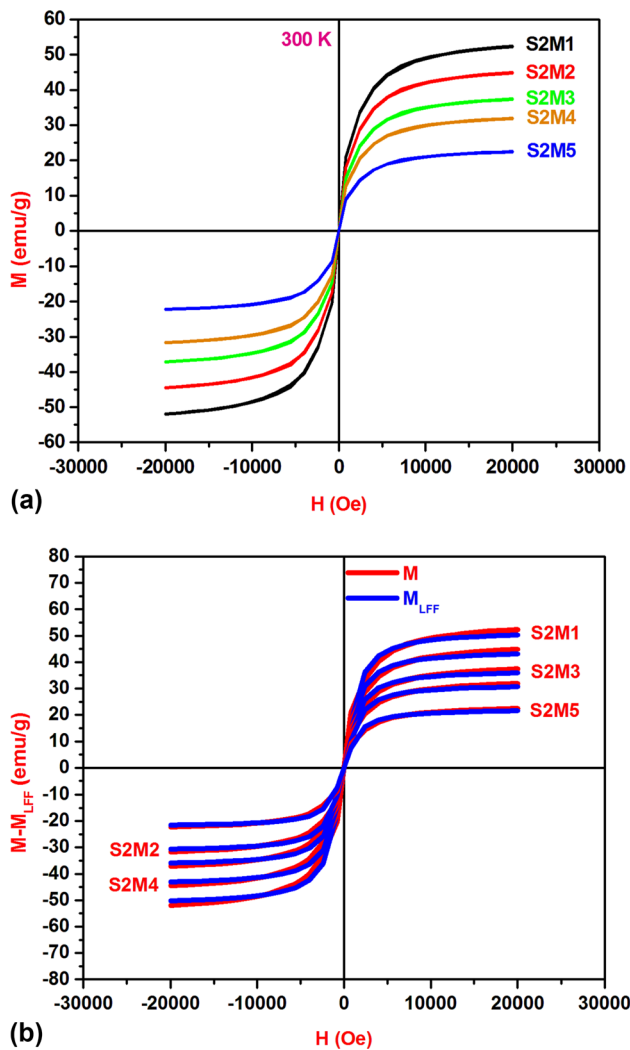

Fig. 8 (a) The 300 K hysteresis loops of the nanosized ferrites S2M1-5 and (b) Langevin function fitted superparamagnetic M-H curves of the nanosized ferrites S2M1-5.

Furthermore, at 300 K, shown in Table IV, the saturation magnetization M_S value 52.24 emu/g of Co$_{0.8}$Ni$_{0.2}$Fe$_2$O$_4$ ($X=0$) seems to be slightly lower than that of the nanosized cobalt ferrite CoFe$_2$O$_4$,[2] 55.97 emu/g and also smaller than that of the CoFe$_2$O$_4$ bulk parent 80.6 emu/g.[43]

In fact, the formation of both shell and core inside magnetic ferrite nanoparticles generated by the surface spin canting orientation impact is primarily induced by magnetic dead layers and spin disordering effects at particle surfaces, which lead to the observed magnitude decrease of saturation magnetization of the five magnetic nanoferrites compared to their CoFe$_2$O$_4$ bulk parent.[44]

However, in 1948, Neel[45] asserted that within the cubic spinel framework AB$_2$O$_4$, the magnetic properties are essentially influenced by the transition metal cation and the statistical repartition between tetrahedral and octahedral sublattice sites. They generate strong predominant dipolar interactions between A and B cations created by their magnetic moment orientations in opposite directions inside their corresponding sublattices whose net magnetic moment magnitude value is calculated by the following equation: $M_L = \sum M_B - \sum M_A$.

Moreover, the M-H curves at 10 K and 300 K exhibit a remarkable decrease in saturation magnetization M_S with copper composition growth between 0 and 0.8, which is mostly dependent on magnetic dipole moment intensity of the transition metal cations inside their corresponding two A and B crystallographic sites. Indeed, inside the nanosized ferrite cubic crystal structure, ferric cations (5 μ_B) are equally distributed between the tetrahedral and octahedral sites, whereas cobaltous (3 μ_B) and nickelous (2 μ_B) cations are only located in the B sites. In addition, during the substitution procedure, Cu^{2+} (1 μ_B) cations preferentially occupy octahedral (B) sites according to the crystal field stabilization energy imposition.[46] Consequently, the calculated net magnetic moment value per molecule, M$_L$, of the five magnetic nanosized ferrites Co$_{0.8}$Ni$_{0.2}$Fe$_2$O$_4$ [2.8 μ_B]; Cu$_{0.2}$Co$_{0.6}$Ni$_{0.2}$Fe$_2$O$_4$ [2.4 μ_B]; Cu$_{0.4}$Co$_{0.4}$Ni$_{0.2}$Fe$_2$O$_4$ [2 μ_B]; Cu$_{0.6}$Co$_{0.2}$Ni$_{0.2}$Fe$_2$O$_4$ [1.6 μ_B]; Cu$_{0.8}$Ni$_{0.2}$Fe$_2$O$_4$ [1.2 μ_B] reveals a decrease with Cu^{2+} composition increase from 0 to 0.8, which causes the saturation magnetization magnitude decrease from 2.8 μ_B to 1.2 μ_B.

Table IV Magnetic properties measured at 10 K and 300 K of the nanosized ferrites S2M1-5

Nanoferrite	10 K			300 K		
	H_c (Oe)	M_r (emu/g)	M_s (emu/g)	H_c (Oe)	M_r (emu/g)	M_s (emu/g)
S2M1	2036	18.69	55.27	0	0	52.24
S2M2	1662	15.70	47.38	0	0	44.77
S2M3	1373	12.84	39.28	0	0	37.12
S2M4	1107	10.68	31.58	0	0	31.82
S2M5	832	7.83	23.69	0	0	22.37

Table V Fit parameter values of M_s(LFF), D(LFF), D_C(LFF), μ_P, K and N_P, with the corresponding R^2 goodness of fit factors of the nanosized ferrites S2M1-5

Nanoferrite	M_s (emu/g)	$M_{s(LFF)}$ (emu/g)	D_{XRPD} (nm)	D_{LFF} (nm)	$D_{C(LFF)}$ (μm)	μ_p (μ_B)	N_P (10^{17}/g)	K×10^5 (erg/cm^3)	R^2
S2M1	52.24	50.27	18.77	16.15	3.660	5748	9.43	4.87	0.9994
S2M2	44.77	43.09	19.97	16.81	4.587	5745	8.08	4.12	0.9994
S2M3	37.12	35.73	20.51	17.08	6.053	5742	6.71	3.39	0.9994
S2M4	31.82	30.62	21.60	17.84	7.592	5738	5.75	2.88	0.9994
S2M5	22.37	21.53	23.39	19.03	12.833	5736	4.04	2.01	0.9994

According to the nanomagnetism theory,[47] the nano-magnetic system can be mostly subdivided into four theory domain states, superparamagnetic domain, single domain, pseudo-single domain and multidomain, which are abbreviated as follows: (SPMD), (SD), (PSD), (MD), respectively. However, the transition from the multidomain to single domain and next to the superparamagnetic domain occurs when the magnetic particle reaches the critical size D_c(LFF) and the superparamagnetic critical threshold size D(LFF), respectively, and considerably depends on the magnitude of magnetocrystalline energy. In addition, when superparamagnetic state is established, magnetic nanoparticles consist of single magnetic domains which are characterized by a special value close to zero of both coercivity and remanence.

The magnetization magnitude mathematical equation, as a function of absolute temperature T and applied magnetic field H $M = M_S \cdot L\left(\frac{\mu_P \cdot H}{K_B \cdot T}\right)$, has been used to calculate the different superparamagnetic parameters described hereafter; the mathematic relation for calculating the magnetic anisotropy constant is $K = \frac{25 K_B T_B}{V}$ and the $D_c = \frac{18\sqrt{AK}}{\mu_0 M_s^2}$ mathematic expression has been used to determine the spherical nanoparticle critical diameter value D_c corresponding to the MD-SD transition.[48] The different variables and constants corresponding to the three equations aforementioned have been well defined in our recent work.[2]

Langevin function fitting (LFF) has been performed by using the recorded 300 K superparamagnetic M-H data, show in Fig. 8b, of the five magnetic nanosized ferrites in order to determine the corresponding superparamagnetic parameters K, N_P, μ_p, D(LFF), D_c(LFF) and M_s(LFF) which are illustrated in Table V.

Furthermore, the listed theoretical calculation data in Table V lead to deduce that the fitted values of both M_s(LFF) and D(LFF) using Langevin function, are in perfect coherence with M_s(300 K) and D(XRPD), as calculated from their corresponding experimental data. The high constant values of magnetocrystalline anisotropy certainly indicate the existence of mutual powerful L-S couplings between Cu^{2+}(1 μ_B), Ni^{2+}(2 μ_B), Co^{2+}(3 μ_B) and Fe^{3+}(5 μ_B) cations within the cubic inverse spinel framework, which show a considerable decrease from 4.87×10^5 erg cm^{-3} to 2.88×10^5 erg cm^{-3} when Cu^{2+} content increases from 0 to 0.8 at Ni^{2+} constant

composition equal to 0.2. Indeed, during the substitution process at Y[Ni^{2+}] content constant equal to 0.2, the increase in Cu^{2+} composition from 0 to 0.8 leads simultaneously to the decrease in Co^{2+} composition from 0.8 to 0. In addition, the presence of magnitude difference in magnetic moment between Cu^{2+}(1 μ_B) and Co^{2+}(3 μ_B) cations induces the observed magnitude decrease in M_S value and thus causes a significant increase in D_C(LFF) value from 3.660 μm to 7.592 μm when Cu content varies from 0 to 0.8. This result is in good agreement with that published recently.[2]

Conclusion

In this study, the five nanosized ferrites, $Co_{0.8}Ni_{0.2}Fe_2O_4$; $Cu_{0.2}Co_{0.6}Ni_{0.2}Fe_2O_4$; $Cu_{0.4}Co_{0.4}Ni_{0.2}Fe_2O_4$; $Cu_{0.6}Co_{0.2}Ni_{0.2}Fe_2O_4$; $Cu_{0.8}Ni_{0.2}Fe_2O_4$, were synthesized by the autocombustion method. The physicochemical characterization data results collected from the Fourier transform infrared, x-ray powder diffraction and DTA-TGA thermal studies have confirmed that the five nanoferrites are pure phases crystallizing in the cubic inverse spinel system and with a crystallite size in the range 19.96–24.94 nm. They remain thermally stable between the combustion temperature and 1173 K, with no detection of tetragonal-cubic phase transition. From the crystallography point of view, the cubic inverse spinel basic structure of these Cu-Ni-Co ferrites remains stable against the substitution process at Ni^{2+} constant content equal to 0.2 when Cu^{2+} composition increases from 0 to 0.8. Moreover, during the Cu-Ni substitution process a decrease has been observed in remanence: M_r(S2M1(X=0))=18.68 emu/g $-M_r$(S2M5(X=0.8))=7.83 emu/g, saturation magnetization: M_s(S2M1(X=0))=55.27 emu/g $-M_s$(S2M5(X=0.8))=23.69 emu/g, coercivity: H_c(S2M1(X=0))=20.36 Oe-H_c(S2M5(X=0.8))=8.32 Oe, blocking temperature: T_B(S2M1(X=0))=282.21 K $-T_B$(S2M5(X=0.8))=267.85 K and magnetocrystalline anisotropy constant: K(S2M1(X=0))=4.87×10^5 erg cm^{-3} $-K$(S2M5(X=0.8))=2.01×10^5 erg cm^{-3}, against an increase in crystalline size values: D_{XRPD}(S2M1(X=0))=18.77 nm-D_{XRPD}(S2M5(X=0.8))=23.39 nm, lattice parameter: a(S2M1(X=0))=8.380(1) Å-a(S2M5(X=0.8))=8.391(3) Å and electrical conductivity which reaches the highest value

18.07×10^{-3} S cm^{-1} associated with the lowest $E_a = 0.360$ eV at 373 K in the case of $Cu_{0.8}Ni_{0.2}Fe_2O_4$.

Furthermore, the SQUID magnetometry measurements have confirmed the presence of 300 K superparamagnetic behavior. Also, theoretical calculations of the superparamagnetic parameters have been performed by using Langevin function fitting on M-H (300 K) data, and the results indicate their remarkable dependence on crystallite size and copper composition impact. The physicochemical characterization results have highlighted the five nanosized ferrite primary features, including strong L-S coupling, excellent electrical conductivity properties, small size exhibiting superparamagnetic behavior at room temperature (300 K), unique ferrimagnetic nature with significant magnetocrystalline anisotropy energy, high homogeneous nanocrystallinity, elevated coercivity value and moderate value of saturation magnetization. These properties make them highly advantageous for various applications in the field of modern nanotechnology.

References

1. W. Belam, Sol–gel chemistry autocombustion synthesis and physicochemical characterizations of the series of Li-Cu cobalt ferrite nanoparticles $LiCu_{(1-2Y)}Co_{(1-Y)}Fe_{(1+2Y)}O_4$. *J. Mol. Struct.* 1209, 127937 (2020).
2. N. Hamdi, L. Bessais, and W. Belam, Sol-gel autocombustion elaboration and physiochemical characterizations of Cu^{2+} substituted cobalt ferrite nanoparticles. *Open Chem. J.* 7, 44 (2020).
3. T. Dippong, E.A. Levei, and O. Cadar, Recent advances in synthesis and applications of MFe_2O_4(M = Co, Cu, Mn, Ni, Zn) nanoparticles. *Nanomaterials* 11, 1560 (2021).
4. I. Sharma and E. Garg, A review on nanoferrites in biomedical applications. *IJBAS* 11(2), 16 (2022).
5. E. Sumalatha, M. Nyathani, T. Anil Babu, D. Ravinder, N.V. Krishna Prasad, and S. Katlakunta, Eco-friendly synthesis, TEM and magnetic properties of Co-Er nano-ferrites. *Biointerface Res. Appl. Chem.* 12, 910 (2022).
6. A. Kumar, T. Gurmeet, and S. Lotey, Synthesis and investigation of structural, optical, magnetic, and biocompatibility properties of nanoferrites $AFeO_2$. *Curr. Appl. Phys.* 27, 103 (2021).
7. X. Wen, F. Zeng, F. Shao, and H. Li, Theoretical study on the application of a Janus CoSTe monolayer for Li-S batteries. *J. Electron. Mater.* 52, 2292 (2023).
8. A.B. Naik, P.P. Naik, S.S. Hasolkar, and D. Naik, Structural, magnetic and electrical properties along with antifungal activity and adsorption ability of cobalt doped manganese ferrite nanoparticles synthesized using combustion route. *Ceram. Int.* 46, 21046 (2020).
9. X. Li, Y. Sun, Y. Zong, Y. Wei, X. Liu, X. Li, Y. Peng, and X. Zheng, Size-effect induced cation redistribution on the magnetic properties of well-dispersed $CoFe_2O_4$ nanocrystals. *J. Alloy Comp.* 841, 155710 (2020).
10. H. Kaur, A. Singh, A. Kumar, and D.S. Ahlawat, Structural, thermal and magnetic investigations of cobalt ferrite doped with Zn^{2+} and Cd^{2+} synthesized by auto combustion method. *J. Magn. Magn. Mater.* 474, 505 (2019).
11. Q.Q. Xiong, J.P. Tu, S.J. Shi, X.Y. Liu, X.L. Wang, and C.D. Gu, Ascorbic acid-assisted synthesis of cobalt ferrite ($CoFe_2O_4$) hierarchical flower-like microspheres with enhanced lithium storage properties. *J. Power Sources* 256, 153 (2014).
12. A. Manikandan, R. Sridhar, S.A. Arul, and S. Ramakrishna, A simple aloe vera plant-extracted microwave and conventional combustion synthesis: morphological, optical, magnetic and catalytic properties of $CoFe_2O_4$ nanostructures. *J. Mol. Struct.* 1076, 188 (2014).
13. H. Ghayour, M. Abdellahi, N. Ozada, S. Jabbrzare, and A. Khandan, Hyperthermia application of zinc doped nickel ferrite nanoparticles. *J. Phys. Chem. Solids* 111, 464 (2017).
14. B. Ozçelik, S. Ozçelik, H. Amaveda, H. Santos, C.J. Borrell, R. Saez-Puche, G.F. de la Fuente, and L.A. Angurel, High speed processing of $NiFe_2O_4$ spinel using laser furnance. *J. Materiomics* 6, 661 (2020).
15. S. Torkian, A. Ghasemi, and R.S. Razavi, Cation distribution and magnetic analysis of wideband microwave absorptive $Co_xNi_{1-x}Fe_2O_4$ ferrites. *Ceram. Int.* 43, 6987 (2017).
16. S. Mallesh, G. Minji, and K.H. Kim, Cubic to tetragonal phase transition in $CuFe_2O_4$ nanoparticles. *J. Magn.* 26(1), 7 (2021).
17. M.A. Shilpa Amulya, H.P. Nagaswarupta, M.P. Anil Kumar, C.R. Ravikumar, K.B. Kusuma, and S.C. Prashantha, Evaluation of bifunctional applications of $CuFe_2O_4$ nanoparticles synthesized by a sonochemical method. *J. Phys. Chem. Solids* 148, 109756 (2021).
18. D. Mohanty, S.K. Satpathy, B. Behera, and R.K. Mohapatra, Dielectric and frequency dependent transport properties in magnesium doped $CuFe_2O_4$ composite. *Mater. Today Proc.* 33, 5226 (2020).
19. S.R. Jain, K.C. Adiga, and V.R. Pai Verneker, A new approach to thermochemical calculations of condensed fuel-oxidizer mixtures. *Combust. Flame* 40, 71 (1981).
20. N. Sanpo, C.C. Berndt, C. Wen, and J. Wang, Transition metal-substituted cobalt ferrite nanoparticles for biomedical applications. *Acta Biomater.* 9, 5830 (2013).
21. U.D. Altermatt and I.D. Brown, A real-space computer-based symmetry algebra. *Acta Cryst. A* 34, 125 (1987).
22. L. Vegard, Die Konstitution der Mischkristalle und die Raumfüllung der Atome. *Z. Phys. Had-rons Nucl.* 5, 17 (1921).
23. K.R. Krishna, D. Ravinder, K.V. Kumar, and Ch.A. Lincon, Synthesis, XRD and SEM studies of zinc substitution in nickel ferrites by citrate gel technique. *World J. Condens. Matter Phys.* 2, 153 (2012).
24. C. Liu, A.J. Rondinone, and Z.J. Zhang, Synthesis of magnetic spinel ferrite $CoFe_2O_4$ nanoparticles from ferric salt and characterization of the size-dependent superparamagnetic properties. *Pure Appl. Chem.* 72, 37 (2000).
25. B. Labde, M.C. Sable, and N. Shamkuwar, Structural and infrared studies of $Ni_{1+x}Pb_xFe_{2-2x}O_4$ system. *Mater. Lett.* 57, 1651 (2003).
26. R.D. Waldron, Infrared spectra of ferrites. *Phys. Rev.* 99, 1727 (1955).

27. A. Samavati and A.F. Ismail, Antibacterial properties of copper-substituted cobalt ferrite nanoparticles synthesized by co-precipitation method. *Particuology* 30, 158 (2017).

28. Z. Shaterabadi, G. Nabiyouni, G.F. Goya, and M. Soleymani, The effect of the magnetically dead layer on the magnetization and the magnetic anisotropy of the dextran-coated magnetite nanoparticles. *Appl. Phys. A* 128, 631 (2022).

29. J.R. Macdonald, *Impedance spectroscopy-emphasizing solid materials and synthesis*, 3rd ed., (New York: Wiley, 1987).

30. B. Madhavilatha, D. Parajuli, K. Jayadev, C. Komali, N. Murali, V. Veeraiah, and K. Samatha, Effect of Cu substitution on magnetic properties of $Co_{0.6}Ni_{0.4}Fe_2O_4$ nanoferrites. *Biointerface Res. Appl. Chem.* 12, 1899 (2022).

31. M. Arifuzzaman and M. BelalHossen, Effect of Cu substitution on structural and electric transport properties of Ni-Cd nanoferrites. *Results Phys.* 16, 102824 (2020).

32. M. Derakhshani, E. Taheri-Nassaj, M. Jazirehpour, and S.M. Masoudpanah, Structural, magnetic, and gigahertz-range electromagnetic wave absorption properties of bulk Ni-Zn ferrite. *Sci. Rep.* 11, 9468 (2021).

33. B.B.V.S. Vara Prasad, K.V. Ramesh, and A. Srinivas, Structural, morphological and magnetic properties of divalent copper-substituted Co-Zn nanoferrites. *Int. J. Mod. Phys. B* 32, 1850172 (2018).

34. K. Vepulanont, S. Sa-Nguanprang, S. Buapoon, T. Bunluesak, P. Suebsom, K. Chaisong, N. Udomsri, N. Karnchana, D. Laokae, and T. Chanadee, Nickel ferrite ceramics: combustion synthesis, sintering, characterization, and magnetic and electrical properties. *Ceram. Soc.* 9, 639 (2021).

35. A.K. Jonscher, The universal dielectric response. *Nature* 267, 267 (1977).

36. W.A. Farooq, M.S. Ul Hasan, M.I. Khan, A.R. Ashraf, M. Abdul Qayyum, N. Yaqub, M. Almutairi, M. Atif, and A. Hanif, Structural, optical and electrical properties of $Cu_{0.6}Co_xZn_{0.4}-xFe_2O_4$ (x = 0.0, 0.1, 0.2, 0.3, 0.4) soft ferrites. *Molecules* 26(5), 1399 (2021).

37. M. Chandel, V. Pratap Singh, R. Jasrotia, K. Singha, and R. Kumar, A review on structural, electrical and magnetic properties of Y-type hexaferrites synthesized by different techniques for antenna applications and microwave absorbing characteristic materials. *AIMS Mater. Sci.* 7, 244 (2020).

38. N. Amri, J. Massoudi, K. Nouri, M. Triki, E. Dhahri, and L. Bessais, Influence of neodymium substitution on structural, magnetic and spectroscopic properties of Ni-Zn-Al nano-ferrites. *RSC Adv.* 11, 13256 (2021).

39. A. Hakeem, T. Alshahrani, G. Muhammad, M.H. Alhossainy, A. Laref, R. Khan, I. Ali, H.M.T. Farid, S.R. Ejaz, and Y. Khosa, Magnetic, dielectric and structural properties of spinel ferrites synthesized by sol-gel method. *J. Mater. Res. Technol.* 11, 158 (2021).

40. A.P. ReenaMary, D. Divya, M.G. Jestin, I. Al Omari, and M.R. Anantharaman, Effect of surfactant mediated inter-particle interactions on the magnetic properties of Manganese Zinc Ferrite ferrofluide. *Mater. Sci. Eng.* 1166, 012027 (2021).

41. U. Klekotka, D. Satuła, S. Spassov, and B. Kalska-Szostko, Influence of atomic doping on thermal stability of ferrite nanoparticles structural and magnetic studies. *Nanomaterials* 14, 100 (2021).

42. A.L. Ribeiro, Characterization of soft magnetic materials using a modified Stoner–Wohlfarth model. *J. Magn. Magn. Mater.* 133, 97 (1994).

43. E. Mazarío, M. Cañete, F. Herranz, J. Sánchez-Marcos, J.M. de la Fuente, P. Herrasti, and N. Menéndez, Highly efficient T2 cobalt ferrite nanoparticles vectorized for internalization in cancer cells. *Pharmaceuticals* 14, 124 (2021).

44. M.S.A. Darwish, H. Kim, H. Lee, C. Ryu, J. Young Lee, and J. Yoon, Engineering core-shell structures of magnetic ferrite nanoparticles for high hyperthermia performance. *Nanomaterials* 10(5), 991 (2020).

45. L. Neel, Propriétés magnétiques des ferrites: ferrimagnétisme et antiferromagnétisme. *Ann. Phys.* 3, 137 (1948).

46. A. Thampi, K. Babu, and S. Verma, Large scale solvothermal synthesis and a strategy to obtain stable Langmuir–Blodgett film of $CoFe_2O_4$ nanoparticles. *J. Alloys Compd.* 564, 143 (2013).

47. T. Nakai, Magnetic domain transition of adjacent narrow thin filim strips with inclined uniaxial magnetic anisotropy. *Micromachines* 11, 229 (2020).

48. L. Néel, Théorie du traînage magnétique des ferromagnétiques en grains fins avec applications aux terres cuites. *Ann. Géophys.* 5, 99 (1949).

Authors and Affiliations

Nabil Hamdi[1] · Wahid Belam[1]

✉ Wahid Belam
  BMWGEM@gmail.com

1   Laboratory of Resources, Materials and Ecosystem,
    Bizerta Science Faculty, Carthage University,
    7021 Jarzouna, Bizerta, Tunisia